INTERNATIONAL JOURNAL FOR NUMERICAL METHODS IN FLUIDS
Int. J. Numer. Meth. Fluids **31**: 681–702 (1999)

ON HIGH-RESOLUTION SCHEMES FOR SOLVING UNSTEADY COMPRESSIBLE TWO-PHASE DILUTE VISCOUS FLOWS

N. THEVAND, E. DANIEL* AND J.C. LORAUD
IUSTI-UMR CNRS 6595, 5 rue Enrico Fermi, 13453 Marseille Cedex 13, France

SUMMARY

A high-resolution numerical scheme based on the MUSCL–Hancock approach is developed to solve unsteady compressible two-phase dilute viscous flow. Numerical considerations for the development of the scheme are provided. Several solvers for the Godunov fluxes are tested and the results lead to the choice of an exact Riemann solver adapted for both gaseous and dispersed phases. The accuracy of the scheme is proven step by step through specific test cases. These simulations are for one-phase viscous flows over a flat plate in subsonic and supersonic regimes, unsteady flows in a low-pressure shock tube, two-phase dilute viscous flows over a flat plate and, finally, two-phase unsteady viscous flows in a shock tube. The results are compared with well-established analytical and numerical solutions and very good agreement is achieved. Copyright © 1999 John Wiley & Sons, Ltd.

KEY WORDS: Eulerian method; two-phase flow; laminar; unsteady

1. INTRODUCTION

Two-phase dilute flows are encountered in many practical situations, such as solid rocket motors, fluidized beds, detonation waves moving near the ground or the transport of pollutants in the atmosphere. When a thermal and dynamical non-equilibrium state between the gaseous phase and the particles exist, governing homogeneous two-phase flow equations are no longer valid. Different approaches are then required in which the gaseous phase and the particles dynamics are described by a specific set of governing equations. Lagrangian [1,2] or Eulerian [3–5] methods are the two possible methodologies. In this study, the Eulerian method is chosen because it seems to be more suitable for unsteady calculations and also less CPU time intensive. The progress of computers not only allows applications that are more complicated to be simulated, from a geometrical point of view, but also the refinement of the physical models. For example, it is now possible to numerically solve the two-phase reactive flow in rocket engines by using sophisticated combustion models of aluminium particles [1,6,7]. In previous approaches, the dissipative effects in the gas phase (viscous flows) are generally included in the models. These effects appear to have a limited influence compared with the drag force or the heat and mass transfer. In these cases, adding these effects is not of great interest.

* Correspondence to: IUSTI-UMR CNRS 6595, 5 rue Enrico Fermi, 13453 Marseille Cedex 13, France.

CCC 0271–2091/99/200681–22$17.50

Received March 1998
Revised June 1998

The subject of this paper is to set up a numerical algorithm to study the two-phase effects on a viscous flow where they are significant near walls. A model is presented to study the interaction between a compressible boundary layer and a dispersed phase. The applications are numerous and are related to the characterization of the boundary layer and its stability, the influence of the dispersed phase on the thrust in a nozzle, etc. Actually, these phenomena are not well-known owing to difficulties encountered validating the models by experimental devices. Nevertheless, some analytical studies have been carried out in the past: one can quote the analytical works on incompressible flows over a flat plate of Marble [8], Soo [9] and Liu [10]. In addition, Osiptsov [11] and Prabha and Jain [12] used numerical models in this field. Considering the compressible flows, Singleton [13] established analytical solutions based on an asymptotic development of the equations of two-phase boundary layer flows for particular cases: (i) when the slip velocity between the gas and the dispersed phase is very large and (ii) for low slip velocity. The model of the interaction between the gas and the particles has been improved by Wang and Glass [14]. They introduced a non-Stokes relation into the interaction between the phases and solved the corresponding set of steady equations.

All these models involve a dilute flow, which means that the volume fraction of the dispersed phase is quite low. The dynamics of such flows are described by partial differential equations that can be identified as transport equations: the gas phase is the carrier and the wave travelling in the dispersed phase propagates along the particle trajectories. However, a mass accumulation is observed near the wall when the relative velocity tends to zero. Some models have been improved to account for the stresses in the dispersed phase due to particle–particle and particle–wall collisions. As for the gas phase, some diffusivity and viscous terms may be included in the equations of the dispersed phase [15,16]. It is obvious that these models are more general than the dilute model, but their exploitation is very difficult. Some parameters have to be experimentally determined, such as the slip wall factor or the particle diffusivity that are still unknown. In this paper, only the dilute flows have been considered.

A general numerical model is proposed which includes unsteady effects. The authors have experience in some second-order numerical schemes of the Lax–Wendroff class, notably the well-known MacCormack one [3,4,17,18], which has been proven very efficient for solving unsteady two-phase dilute flows. This method requires additional second- and fourth-order artificial viscosities in order to avoid spurious oscillations. These terms involve various constant coefficients depending on the phase (gaseous or dispersed) and require numerous numerical experiments: the generality of such a method vanishes because of these arguments. Among the well-tested methods used today, the second-order finite volume methods verifying the TVD condition are preferred. An imposed constraint on the present problem is to use the same numerical scheme for both the gaseous and the dispersed phase in order to improve the computational efficiency and to maintain consistent numerical errors for both phases.

By using a finite volume method, the fluxes have to be solved by means of exact or approximate Riemann solvers. For the gas that is assumed to obey the ideal gas law, many solvers exist and some of them will be tested in this paper. For the dispersed phase, one can use an exact solver proposed in Reference [5]. One can also quote the work of Sainseaulieu [19], who proposes an approximate solver based on a Roe decomposition for the two-phase flow equations. The last method has the drawback of introducing an artificial modification into the governing equations to turn the system of partial differential equations into a hyperbolic one. Both methods are robust but the first is chosen for the present study. The Donor–Cell methods are not retained because they are not accurate enough (first-order) and too dissipative for such studies. Then, a flux limiter function must be employed to obtain a TVD scheme.

In this paper, the two-phase dilute flows governing equations are firstly presented and then the numerical scheme based on the MUSCL–Hancock method [20–22] is developed. A particular effort is made on the choice of the solver and the limiter function. The numerical test cases are first related to a one-phase viscous flow calculation for which some analytical solutions exist. These test cases include steady or unsteady solutions at low Mach number or supersonic flow regimes. The steady two-phase flow numerical solutions are compared with some analytical results or with published results. The influence of the particles on the boundary layer will be illustrated on typical quantities.

2. GOVERNING EQUATIONS

The general unsteady two-phase dilute flow equations are given hereafter. A system of partial differential equations (PDE) is written without being established. These equations are classical [3,4,23,24], thus only the assumptions are reviewed. Considering a dilute flow means that the volume fraction of the dispersed phase is low. As a consequence, there is no pressure term in the dispersed phase equations. The coupling between the gas and the particles is only due to the two-phase exchanges as the drag force and the heat transfer. These effects appear as source terms in the system of equations. Moreover, each phase is considered as a continuous media and the specific assumptions are:

- the flow is two-dimensional (or axisymmetric) and unsteady,
- the gas is compressible and obeys the ideal gas law,
- the fluid is viscous,
- the particles are solid and spherical,
- the temperature within a particle is uniform,
- the drag force and the heat transfer between the two phases are considered.

The system of equations is deduced from the general balances of mass, momentum and energy, and is given in conservative form:

$$\frac{\partial U}{\partial t} + \vec{\nabla}\cdot(\vec{F} - \vec{F}_v) = Q,$$

with

$$U = \begin{bmatrix} \rho \\ \rho\vec{V} \\ \rho E \\ \rho_p \\ \rho_p\vec{V}_p \\ \rho_p E_p \end{bmatrix}, \qquad \vec{F} = \begin{bmatrix} \rho\vec{V} \\ \rho\vec{V}\vec{V} + P\bar{\bar{I}} \\ \rho H\vec{V} \\ \rho_p\vec{V}_p \\ \rho_p\vec{V}_p\vec{V}_p \\ \rho_p E_p\vec{V}_p \end{bmatrix},$$

$$\vec{F}_v = \begin{bmatrix} 0 \\ \bar{\bar{\tau}} \\ \bar{\bar{\tau}}\cdot\vec{V} + k\vec{\nabla}T \\ 0 \\ 0 \\ 0 \end{bmatrix}, \qquad Q = \begin{bmatrix} 0 \\ \vec{F}_{g-p} \\ Q_{g-p} + \vec{F}_{g-p}\cdot\vec{V}_p \\ 0 \\ -\vec{F}_{g-p} \\ Q_{g-p} \end{bmatrix}.$$

In this system, ρ_p is the apparent density defined by $\rho_p = n_p \frac{4}{3}\pi R_p^3 \rho^*$, ρ^* is the material density, n_p the number of particles per unit mixture volume and R_p is the particle radius.

The classical Newtonian law gives the stress tensor

$$\tau_{ij} = \mu(\vec{\nabla}\vec{V} + (\vec{\nabla}\vec{V})^T) - \frac{2}{3}\mu(\vec{\nabla}\cdot\vec{V})\delta_{ij} = \mu(\partial_i v_j + \partial_j v_i) - \frac{2}{3}\mu(\partial_i v_i + \partial_j v_j)\delta_{ij},$$

where μ denotes the kinematic viscosity and varies with the temperature according to Sutherland's law for air:

$$\mu = 1.458 \times 10^{-6} \frac{T\sqrt{T}}{(T + 110.4)}.$$

Stokes law gives the drag force, indeed the ratio ρ/ρ_p is small enough to assume that this force is much larger than other ones (Basset, virtual mass, . . .). Then, the term $\vec{F}_{q-p}$ is given by

$$\vec{F}_{g-p} = n_p C_d \frac{1}{2}\rho\pi R_p^2 \| \vec{V}_p - \vec{V} \| (\vec{V}_p - \vec{V}),$$

with C_d being the drag coefficient equal to [25]

$$C_d = \frac{1}{50} Re_p + \frac{7}{6} Re_p^{0.15}.$$

Only the convective heat transfer is considered around an isolated particle, so the heat transfer coefficient h in the relation $Q_{g-p} = n_p 4\pi R_p^2 h(T - T_p)$ is obtained with a correlation of the Nusselt number, namely [26]:

$$Nu = \frac{2hR_p}{\lambda} = 2 + 0.6 Re_p^{1/2} \cdot Pr^{1/3},$$

where Re_p is the particle Reynolds number based on the relative velocity and the particle diameter. The other quantities obey the usual notations.

3. NUMERICAL SCHEME

The use of a high-order scheme appears to be a necessity to solve accurately the unsteady Navier–Stokes equations coupled with the dilute flow equations. Some gradients obviously exist in the boundary layer of the gas but also in the dispersed phase. Such methods produce unphysical oscillations, which vanish by introducing a total variation diminishing (TVD) property. The use of the MUSCL approach, presented by Van Leer [21], seems appropriate to solve this set of equations; the TVD property is obtained by the limitation of slopes of the conservative variables. The MUSCL–Hancock [22,23] method is used to solve the set of PDE. This method is widely used for classical hyperbolic system (Euler equations), but less common for viscous flows and for two-phase dilute flows. Moreover, the viscous fluxes are not treated by the splitting of the global set of equations [23] as generally proposed, but directly integrated in the PDE solver. Nevertheless, the scheme is split to separate the convective part of the PDE and the source terms that are integrated over a time step by using an ODE solver. The following operators are defined:

$$L_{\text{conv}}(U^n) = \tilde{U} \text{ where } \tilde{U} \text{ is the solution of } \frac{\partial U}{\partial t} + \vec{\nabla}\cdot(\vec{F} - \vec{F}_v) = 0, \tag{1}$$

$$L_{\text{sour}}(\tilde{U}) = U^{n+1} \text{ where } U^{n+1} \text{ is the solution of } \frac{\mathrm{d}\tilde{U}}{\mathrm{d}t} = Q(U^n). \tag{2}$$

The L_{sour} operator is an ODE solver such as Runge–Kutta.

The MUSCL–Hancock method is based on a three-step decomposition: extrapolation of variables with an updating at time $t + (\Delta t/2)$, calculation of the fluxes and time integration over a cell (conservation stage). The three steps are detailed hereafter.

3.1. Data reconstruction

The values U_{ij} are extrapolated at the cell faces by using a linear approximation of the conservative variables over the cell. This approximation is controlled by non-linear slope limiters to obtain a second-order oscillation-free solution (TVD property).

$$U^L_{i+1/2,j} = U_{ij} + \frac{1}{4}[(1-k)\Phi^+_{i-1/2}(U_{ij} - U_{i-1,j}) + (1+k)\Phi^-_{i+1/2}(U_{i+1,j} - U_{ij})], \tag{3}$$

where

$$\Phi^+_{i-1/2} = \Phi\left(\frac{U_{i+1,j} - U_{ij}}{U_{ij} - U_{i-1,j}}\right), \qquad \Phi^-_{i+1/2} = \Phi\left(\frac{U_{ij} - U_{i-1,j}}{U_{i+1,j} - U_{ij}}\right),$$

and

$$U^{\mathrm{R}}_{i+1/2,j} = U_{i+1,j} - \frac{1}{4}[(1+k)\Phi^+_{i+1/2}(U_{i+1,j} - U_{ij}) + (1-k)\Phi^-_{i+3/2}(U_{i+2,j} - U_{i+1,j})],$$

where

$$\Phi^+_{i+1/2} = \Phi\left(\frac{U_{i+2,j} - U_{i+1,j}}{U_{i+1,j} - U_{i,j}}\right), \qquad \Phi^-_{i+3/2} = \Phi\left(\frac{U_{i+1,j} - U_{i,j}}{U_{i+2,j} - U_{i+1j}}\right).$$

Here, k is a free parameter in the range $[-1, 1]$. The scheme is totally upwind if $k = -1$ or centred if $k = 1$. This parameter disappears when a symmetrical slope limiter is used. Several slope limiters have been tested in order to find which one would lead to the most accurate scheme. Some usual slope limiters are expressed [23,27]:

Symmetrical slope limiter:

Minmod: $\Phi(r) = \max(0, \min(r, 1))$,
Superbee by Roe: $\Phi(r) = \max(0, \min(2r, 1), \min(r, 2))$,
Van-Leer: $\Phi(r) = (r + |r|)/(1 + r)$,
Van-Albada: $\Phi(r) = (r^2 + r)/(1 + r^2)$.

Non-symmetrical slope limiter:

Chakravarthy, Osher: $\Phi(r) = \max(0, \min(r, \beta)), \quad 1 \le \beta \le 2.$

Then, for each cell, the boundary extrapolated values $U_{i\pm1/2,j}$, $U_{i,j\pm1/2}$ and the average value $U_{i,j}$ are evolved over a half time step,

$$U^{n+1/2}_{i+1/2,j} = U^n_{i+1/2,j} - \frac{1}{2}\frac{\Delta t}{\Omega_{ij}}\sum_{k=1}^{4}(\vec{F}_k \cdot \vec{n}_k). \tag{4}$$

This evolution is only concerned with the convective effects and is entirely contained in each cell. It means that the viscous fluxes are not included in this step.

3.2. Flux calculation

The fluxes are divided into the inviscid and the viscous parts. A conventional, exact or approximate Riemann solver is used to compute the inviscid flux, i.e. $F_{i+1/2}$. The calculation is based on the data $U^{\mathrm{L}}_{i+1/2}$ and $U^{\mathrm{R}}_{i+1/2}$. The superscripts L and R denote the left and the right states on both sides of the interface. Several solvers have been tested: the exact Riemann solver, some approximated Riemann solvers, the HLLC scheme, as well as the SLIC scheme, which is a second-order extension of the FORCE scheme. The solution of the Riemann problem is well-documented in the scientific community and not repeated here. However, the reader could refer to the recent book from Toro [23].

The inviscid boundary conditions are applied by setting up a layer of ghost cells along each of the boundaries. For an inflow boundary, all of the ghost cell quantities are fixed while for an outflow boundary, the ghost cell quantities are extrapolated from the nearest calculated values. Tangency boundary conditions are applied by setting all of the scalar quantities in the ghost cells equal to those in the active cells adjacent to the boundary, but setting the ghost cell velocities to the mirror image of those in the active cells.

The viscous fluxes are integrated by a different method than the inviscid flux. There are no analytical relations such as the Rankine–Hugoniot equations, and they essentially involve some derivatives versus the space co-ordinates that are not easy to calculate without damaging the finite volume approach.

According to Equation (1), the viscous fluxes are required on the cell faces. The viscous flux on side AB (Figure 1) is defined as

$$F_{v,\mathrm{AB}} = \frac{(F_{v,\mathrm{A}} + F_{v,\mathrm{B}})}{2}.$$

The derivatives of temperature and velocity required for the stress tensor are evaluated in the cell corners, namely A and B. A secondary mesh has to be define over the main grid. The initial centres of cells become the corners of the new grid (Figure 1).

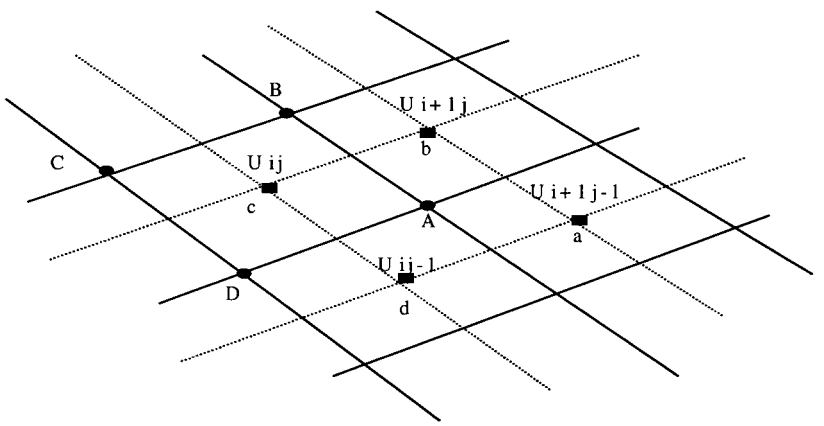

Figure 1. Primary (●) and secondary (■) mesh.

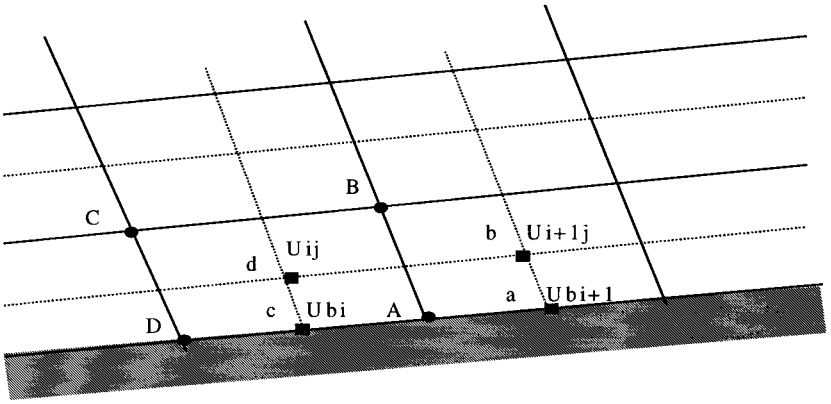

Figure 2. Primary (●) and secondary (■) mesh near the wall.

The divergence theorem is then applied to obtain the expression of spatial derivatives. For example, the x derivative of the variable U at point A is defined by

$$\left(\frac{\partial U}{\partial x}\right)_{\mathrm{A}} = \frac{1}{\Omega_2}\oint_{\Omega_2}\frac{\partial U}{\partial x}\,\mathrm{d}y = \frac{\oint_{S_2} U\,\mathrm{d}y}{\oint_{S_2} x\,\mathrm{d}y} = \frac{(U_\mathrm{a}-U_\mathrm{c})\cdot(y_\mathrm{b}-y_\mathrm{d})-(U_\mathrm{b}-U_\mathrm{d})\cdot(y_\mathrm{a}-y_\mathrm{c})}{(x_\mathrm{a}-x_\mathrm{c})\cdot(y_\mathrm{b}-y_\mathrm{d})-(x_\mathrm{b}-x_\mathrm{d})\cdot(y_\mathrm{a}-y_\mathrm{c})},$$

where Ω_2 is the volume of the cell abcd and S_2 is the contour surface. The ratio of cell stretching is limited to 8% to insure good accuracy in the computation of the derivative, when a non-regular meshing is used. Thus, the location of point A is very close to the centre of the volume Ω_2, which leads to good accuracy for this approximation [27].

For cells close to the mesh boundary, values of the variable U are imposed at the cell corners (Figure 2). The values given to U depend on the nature of the boundary. For a no-slip wall boundary, the velocity components are set to zero. The temperature is extrapolated or fixed depending on whether the wall is adiabatic or not. For inflow, outflow or tangency boundaries, the values are left as computed at the first step. With this methodology, there is no use of ghost cells for the viscous terms. The average values used at this step are based on the average ones calculated at the evolution step.

3.3. Conservation step

The third step is the final integration of the finite volume formula given by (1). This stage is classical and no particular comment is necessary.

4. RESULTS

4.1. Introduction

The MUSCL–Hancock scheme is widely used in the CFD community, but primarily in the field of one-phase flows. The extension to unsteady viscous two-phase flows is very unusual. One of the advantages of this methodology lies in the large span of Riemann solvers that can be used to calculate the inviscid fluxes. One has the choice between approximate or exact

solvers. Most of them have been tested and those found to be more attractive for the concerned problem are presented.

The method developed is explicit so a restriction on the time step is required. The dispersed phase characteristic time was always greater than the gaseous one, and then the classical CFL criterion is sufficient to insure the stability of the scheme in the following calculations. The time step is actually defined as the smallest value of

$$\Delta t = \sigma\left(\frac{1}{\Delta t_1}+\frac{1}{\Delta t_2}+\frac{1}{\Delta t_{\text{viscous}}}\right)^{-1}$$

for each cell, where σ is a security coefficient,

$$\frac{1}{\Delta t_{1,2}} = \frac{|v_{1,2}|+a}{L_{1,2}}$$

are the inviscid signal frequencies along interfaces of length L in each direction and

$$\frac{1}{\Delta t_{\text{viscous}}} = \frac{4\mu\gamma}{Pr\rho}\left(\frac{1}{L_1^2}+\frac{1}{L_2^2}\right)$$

is an approximation of the viscous limit [28]. The value of σ is fixed at 0.9.

4.1.1. About the Riemann solver. A solver gives the characteristic values of the flow at the cell interface as the solution of a Riemann problem. The solution is a non-linear one, linking the left and the right state on both sides of an interface. If the solution is reduced to an algebraic formula it can be written, but for the other cases the reader should refer to the relevant articles. It is assumed that the local solution is one-dimensional along a cell face.

The centred SLIC solver, defined from the flux force [23], is first examined. The solution is algebraic:

$$F^{\text{SLIC}}_{i+1/2} = F^{\text{FORCE}}_{i+1/2}(W^{\text{L}}, W^{\text{R}}) = \frac{1}{2}[F^{\text{RI}}_{i+1/2}(W^{\text{L}}, W^{\text{R}}) + F^{\text{LF}}_{i+1/2}(W^{\text{L}}, W^{\text{R}})].$$

In this expression, $F_{i+1/2}$ denotes the solution at an interface located at $i+1/2$, F^{RI} being the Richtmyer's flux, F^{LF} the Lax–Friedrichs's flux and W the vector of the primitive variables of the system. The different fluxes are defined as:

$$F^{\text{RI}} = F(U^{\text{RI}}) \text{ with } U^{\text{RI}} = \frac{1}{2}(W^{\text{L}}+W^{\text{R}}) + \frac{1}{2}\frac{\Delta t}{\Delta x}(F(W^{\text{L}}) - F(W^{\text{R}}))$$

and

$$F^{\text{LF}} = \frac{1}{2}(F(W^{\text{L}}) + F(W^{\text{R}})) + \frac{1}{2}\frac{\Delta x}{\Delta t}(W^{\text{L}} + W^{\text{R}}).$$

This solver was the first examined because of evident advantages. It can be applied whatever the considered phase and the algebraic formulation require no iterative procedure. Actually, some difficulties arose when two-dimensional problems were solved because some instabilities appeared when waves propagate along directions different from the grid directions. Moreover, the dissipation dominates when the solver is applied to the dispersed phase.

The more suitable solution is to compute the numerical fluxes with appropriate solvers for each phase. For the gas phase, the HLLC solver, the double rarefaction or double compression solver and an exact Riemann solver [22] are introduced into the numerical model. These solvers are easy to build as soon as the equation of state is known (here, the ideal gas law). As

a final choice, an exact solver is used. Indeed, the very useful HLLC solver shows some instabilities in particular configurations, such as two-phase nozzle flows. The other approximate solvers also give good results but the expected CPU time saving is not high enough compared with an exact solution. For the dispersed phase the fluxes are computed from the solution given in Reference [5].

As an example, a classical test case for the dispersed phase is carried out. It only involves the particle equations with no source term. A squared signal of the density is moving with a constant velocity. The propagation of a signal in the range $\rho_p = [0; 1]$ was first computed but led to negative values of ρ_p with SLIC solver. On the other hand, the exact solver preserved the positivity. This property is very important because the diameter of particles is deduced from the value of ρ_p. In Figure 3 results for the signal in the range $\rho_p = [0.1; 1]$ are presented for both solvers.

4.1.2. About the limiters. The method is based on the use of a non-linear slope limiter to avoid non-physical oscillations. In the two-phase approach, the use of the same limiter is prescribed in order to obtain the same numerical errors, which enforce the consistency of the scheme. Many test cases with inviscid two-phase flows have been performed with the numerical scheme that are not reported here. These test cases are related to acoustic waves propagating in one- and two-phase flows that are defined in References [17,18]. The analysis of the results leads to the use of the Van-Leer and Van-Albada symmetrical limiters or the non-symmetrical Chakravarthy and Osher limiter. The Minmod limiter generates excessive numerical dissipation to obtain accurate results. The Superbee-Roe limiter leads to an accurate capture of a discontinuity but may unfortunately yield unphysical oscillations that are very dramatic for the dispersed phase.

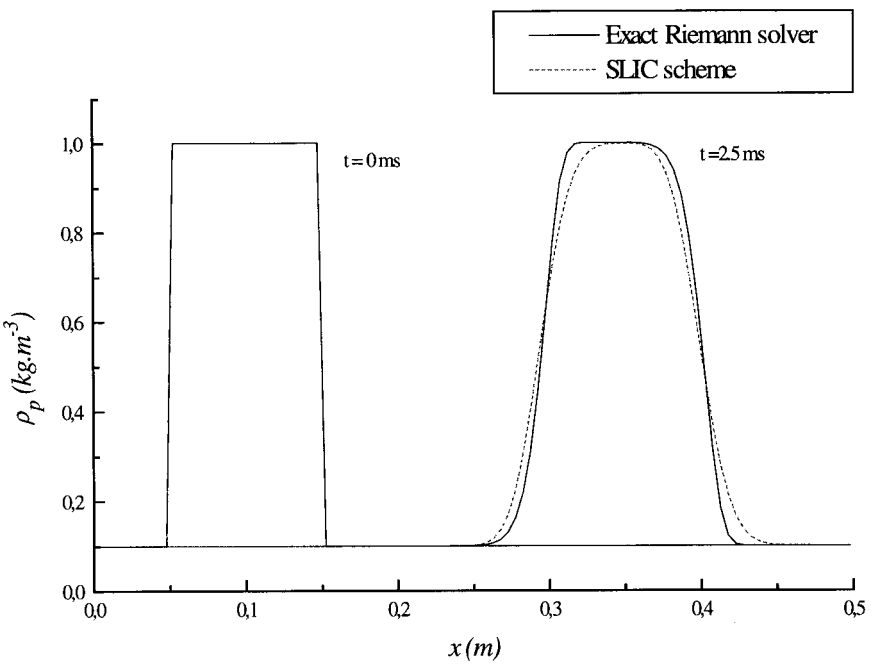

Figure 3. Translation of a squared density signal.

For these preliminary comments to be advanced, the numerical model has to be validated. There is no problem in doing this for the gaseous phase because numerous analytical or numerical solutions are available in a large range of the flow regime. On the contrary, there are only a few test cases that allow the validation of the dispersed phase behaviour in viscous flows.

The methodology employed here is given below. The ability of the numerical scheme to solve one-phase viscous flows is checked by the calculation of the steady boundary layer in a subsonic and a supersonic regime. A viscous shock tube problem is solved in order to appreciate the development of the boundary layer in the unsteady regime. Classical results are then pointed out. Then, the validation for two-phase flow simulations is presented. A few results may be found in the literature, but they are compared with those obtained with the developed methodology. The comparisons are about steady and unsteady two-phase flows.

4.2. Laminar boundary layer of a pure gas over a flat plate

The laminar boundary layer over a flat plate is a popular test problem because analytical solutions can be found in the literature, such as Blasius [29,30], and also numerical solutions. Two test cases are presented, the first one is a subsonic flow and the other one a supersonic flow.

4.2.1. Subsonic flow over a flat plate. The Blasius equations allow the calculation of the steady profiles in an incompressible boundary layer over a flat plate. The flows studied here are compressible but the choice of an upstream Mach number equal to 0.3 leads to a quasi-incompressible flow; the ratio of the density at the exit of the domain over the density at the inlet is 97%. This result is quite acceptable to assume negligible compressibility effects and to compare the results with the Blasius solution.

The computational grid is composed of 50×60 cells and is presented in Figure 4. The mesh is stretched in the y-direction in view to obtain an accurate calculation of the boundary layer. In the computational domain, the flat plate begins at the third cell; upstream conditions may then be set before this point and some oscillations are avoided. From the third cell, the described boundary conditions for a wall are computed.

The slope limiter used in this test case is the non-symmetrical Chakravarthy and Osher limiter with the adjustable parameters fixed at $k = \frac{1}{3}$ and $\beta = 2$.

Results are provided using the classical dimensionless Blasius variables: $\eta_B = y(u_e/\nu x)^{1/2}$ where u_e is the flow velocity in the external free stream and ν is the fluid kinematic viscosity. The normal and tangential velocities are expressed in non-dimensional form as

$$u^* = \frac{u}{u_e}, \qquad v^* = \frac{v}{u_e} Re_e^{1/2},$$

where Re_e is the external Reynolds number based on the distance from the plate leading edge. Figure 5 shows a comparison between the computed velocity profiles and the profiles computed from the Blasius solution.

The two sets of profiles are very close and the tangential velocity is perfectly described. A deviation appears in the normal component profile but is relatively small.

The wall friction factor, which is of practical interest for determining the strength imposed to material structures, is also calculated. The definition is

$$C_f = \frac{\tau_W}{\frac{1}{2}\rho_e u_e^2}, \quad \text{with } \tau_W = \mu_W \left(\frac{\partial u}{\partial y}\right)_{\text{Wall}}.$$

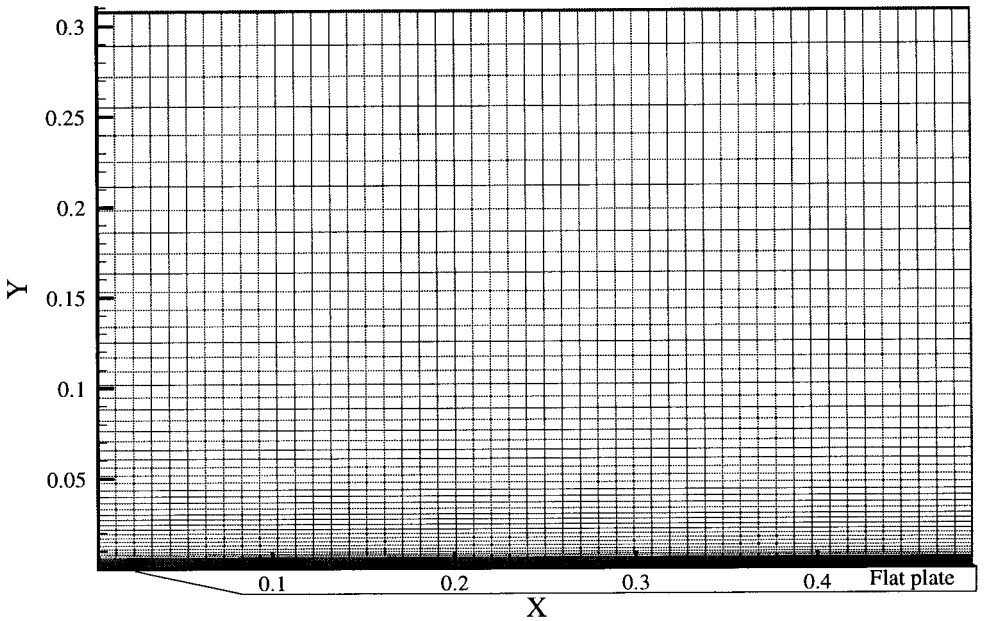

Figure 4. Computational mesh for the Blasius test problem.

The comparison between numerical and analytical solutions, shown in Figure 6, gives good agreement.

This test case, far from being a comprehensive check of the Navier–Stokes solver, shows the good agreement between the analytical and the numerical solution. This test case is relatively difficult because it involves solutions in the limit of compressible flow.

4.2.2. Supersonic flow over a flat plate. The test case proposed here is a very complete one: it allows the solution of thermal and dynamical boundary layers and involves a shock wave. Indeed, for a supersonic viscous flow at Mach number equal to 2, the interaction with a flat plate at fixed temperature produces thermal and dynamic boundary layers as well as a leading edge interaction shock (LEIS). Unfortunately, exact or analytical solutions are not available for the LEIS; consequently, the numerical results proposed by Jacobs [28] are drawn heavily upon.

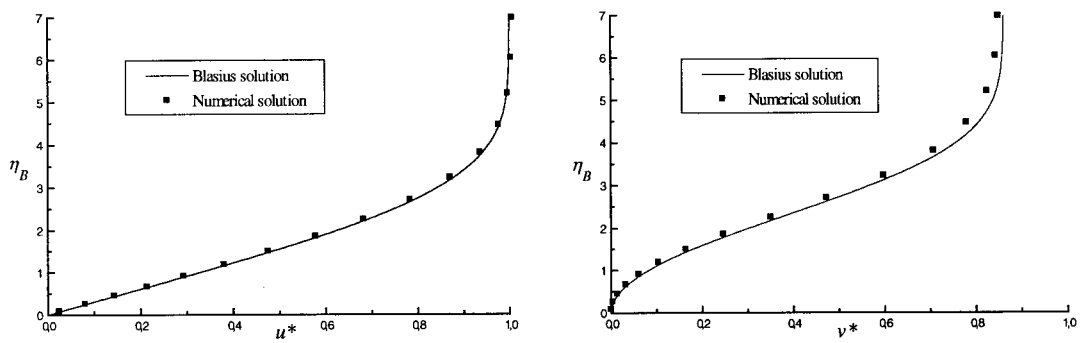

Figure 5. Velocity profiles.

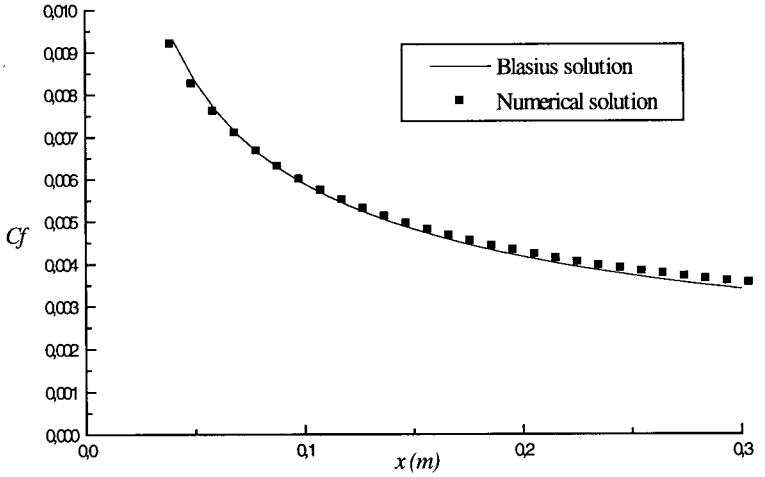

Figure 6. Wall friction factor.

The external free stream is defined as follow: $u_e = 597.3$ m s^{-1}, $\rho_e = 4.04 \times 10^{-3}$ kg m^{-3}, $T_e = 222$ K. Figure 7 shows the computational mesh used for this test. It is composed of 50×50 cells and stretched in the x and y-directions, in a view to optimize the capture of the boundary layer. The shape of the mesh is designed to include the LEIS in the computational domain. The south boundary is a no-slip wall with a fixed temperature $T_w = 222$ K. The non-symmetrical Chakravarthy and Osher limiter with the parameters $k = \frac{1}{3}$ and $\beta = 2$ is used for this test.

In Figure 8, the profiles of velocity and temperature are given at $x = 0.85$ m from the leading edge. These profiles, as well as the LEIS pressure contours (Figure 9), are similar to those provided by Jacobs [28]. The results show a maximum temperature of 258 K due the work of the shear stress forces. The dynamic boundary layer thickness reaches 1.3 mm. The good agreement with the numerical results obtained by Jacobs adds credence to the construction of the scheme. It is interesting to compare the numerical results in the boundary layer with the analytical self-similar Crocco solution. The latter gives an exact relation between the enthalpy and the velocity. In Figure 10, a good agreement between both solutions is observed, with no discernible differences found.

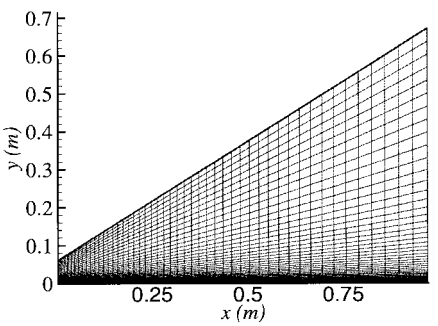

Figure 7. Computational mesh.

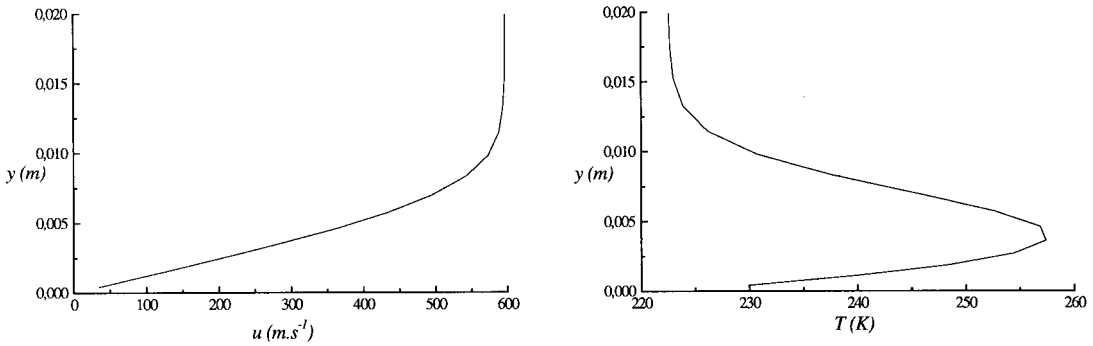

Figure 8. Velocity and temperature profiles.

This test case is relatively comprehensive and the results are very satisfying. At this point, the ability of the scheme to describe steady one-phase flows is verified.

4.3. Viscous flow in a low-pressure shock tube

This test is performed to study the development of a boundary layer in a shock tube and its effects on the wave propagation. The aim is to show the ability of the scheme to simulate unsteady one-phase flows. The axisymmetrical equations are solved here.

In shock tube flow, the presence of a boundary layer causes the shock to slow down, the contact surface to accelerate and the flow to be non-uniform. Indeed, the wall boundary layer acts as an aerodynamic sink removing mass from the region between the shock and the contact surface. As the shock tube length-to-diameter ratio is increased and as the initial pressure in the low-pressure section is reduced, the wall boundary layer effects become more pronounced [31].

A computational domain is designed to simulate the flow in a 1 m long tube whose diameter is 5.4×10^{-3} m. A diaphragm separates the domain in two regions corresponding to the high and low pressure parts of the tube. The initial pressures are fixed at 0.14 and 0.02 bar respectively. The temperature in both sections corresponds to standard state conditions. The pressure ratio produces a Mach number equal to 4, with a shock wave propagating in the low-pressure region, followed by a contact discontinuity. At the same time, an expansion fan moves to the left in the high-pressure section.

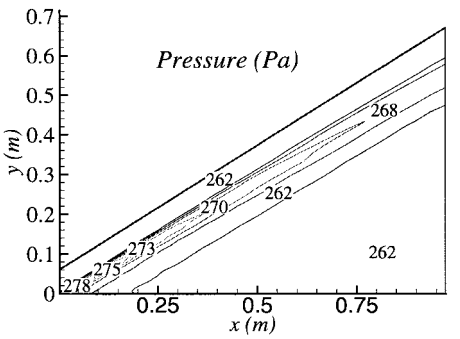

Figure 9. LEIS.

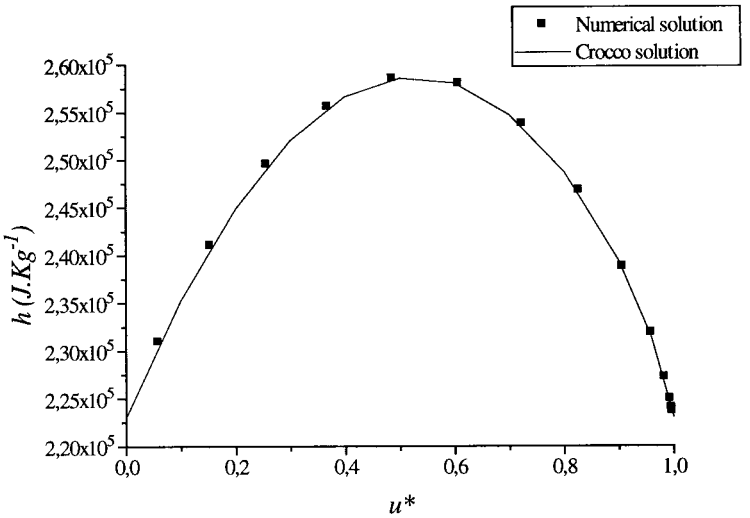

Figure 10. Comparison with the Crocco relation.

The computation is performed on a 200×35 mesh stretched in the y-direction. The x co-ordinate corresponds to the tube axis. The north boundary (wall) is endowed with adiabatic no-slip wall boundary conditions. The limiter used for this computation is the Van-Leer one and then a numerical dissipation appears at the different discontinuities. The shock is consequently captured in four points and the contact surface in six points. This dissipation is low by reference to the mesh size and the separation distance between the waves. It will not dramatically affect the result of this simulation.

Figure 11 shows enlarged velocity contours at different times. The development of the boundary layer and its effects on the external flow can be observed. Unlike an ideal gas flow, the viscous one appears to be non-uniform. The flow velocity increases between the rarefaction wave and the discontinuity surface then decreases between this last one and the shock wave. In agreement with experimental observations and analytical analysis, the contact discontinuity accelerates and the shock wave decelerates, as shown in Figure 12. In this x–t diagram, the classical solution (Euler's solution) is drawn in solid lines while the viscous solution is plotted in dashed lines. The positions are obviously measured on the axis far from the boundary layer.

This last simulation proved that the numerical scheme is able to calculate the unsteady development of a boundary layer. It is clear that the method is very suitable for one-phase steady and unsteady flows. The ability of the method to solve two-phase dilute flows is now demonstrated.

4.4. Two-phase flow over a flat plate

Considering a two-phase flow greatly changes the mean features of the boundary layer over a flat plate. The heat transfer and the drag force between the gas and the particles imply some consequent modifications in the analysis. Classically, three different regions are defined in the two-phase boundary layer, which can be distinguished by the relative velocity between both phases (Figure 13). A large-slip region close to the leading edge (I), a moderate-slip region (II) and a small-slip one far downstream (III) [11,14]. The characteristic scale in this two-phase flow problem is the relaxation length λ_e, defined from the particle dynamical relaxation time:

$$\lambda_e = \frac{\rho_S \cdot d^2 \cdot u_e}{18\mu_e},$$

where ρ_e and μ_e are the density and kinematic viscosity of the gas in the external flow; ρ_S and d are the material density and the diameter of particles. The three regions are defined according to the order of magnitude of the slip parameter $x^* = x/\lambda_e$.

A test case is now defined and will be solved numerically. The free stream flow is defined by the Reynolds number, Re_p, based on the particle diameter.

$$Re_p = \frac{\rho_e \cdot u_e \cdot d}{\mu_e}.$$

The particle Reynolds number Re_p is assumed to be equal to 10 with a constant particle diameter d equal to 10 μm. The material density of particles is 1766 kg m^{-3}. The Prandtl number is equal to 0.75. The computation has been performed on a rectangular 70×70 cells mesh stretched in the y-direction. The south boundary (wall) is treated as a no-slip wall boundary for the gas phase: both components of the gas velocity are set to zero, while the particle phase encounters slip wall conditions. The normal fluxes are set to zero. Unlike the gas phase, there is no exchange of momentum or energy between the dispersed phase and the wall. The gas and the particles enter the computational domain under thermal and dynamical equilibrium conditions. The non-symmetrical Chakravarthy and Osher slope limiter with the parameters $k = \frac{1}{3}$ and $\beta = 2$ is used for this computation.

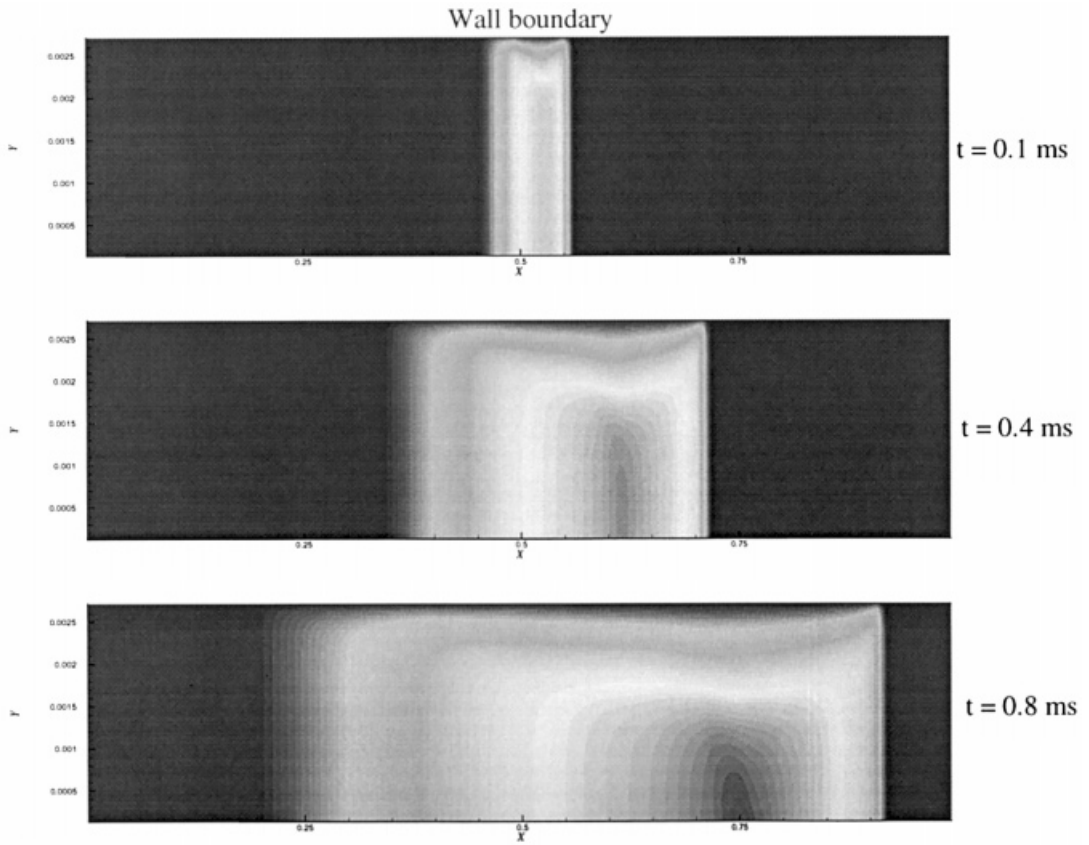

Figure 11. Velocity contours.

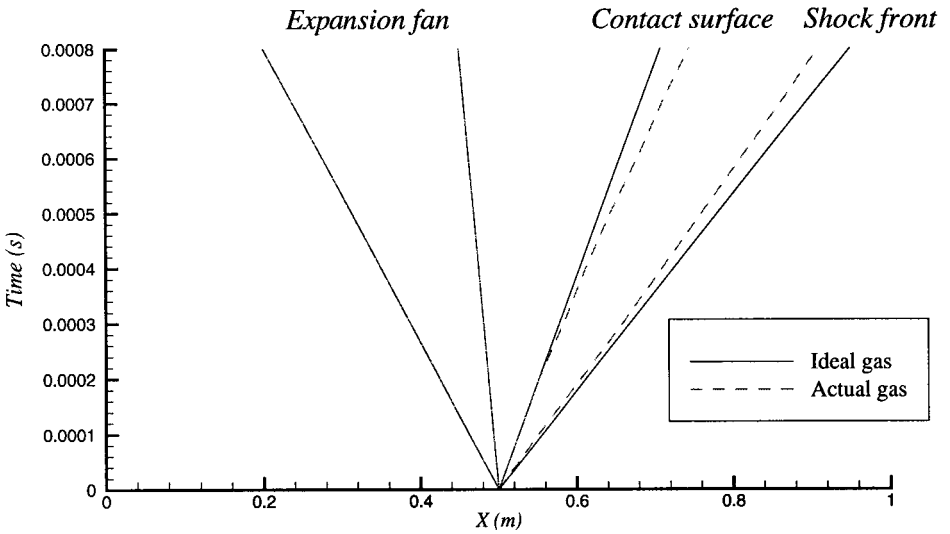

Figure 12. Waves in a shock tube.

The following dimensionless variables are introduced in order to bring all quantities to the same order of magnitude:

$$x^* = \frac{x}{\lambda_e}, \quad u^* = \frac{u}{u_e}, \quad u_p^* = \frac{u_p}{u_e}, \quad y^* = \frac{y}{\lambda_e} Re^{1/2}, \quad v^* = \frac{v}{u_e} Re^{1/2}, \quad v_p^* = \frac{v_p}{u_e} Re^{1/2},$$

where Re is now the Reynolds number based on λ_e,

$$Re = \frac{\rho_e \cdot u_e \cdot \lambda_e}{\mu_e}.$$

Figure 14 shows the results for the steady flow. The figure provides the development of gas and particles velocity profiles within the three regions mentioned earlier.

$x^* = 0.1$: In the near-leading edge area, the gas velocity is adjusted at the wall to obtain the no-slip condition as for the case of a pure gas boundary layer. The particles have no time to adjust to the local gas motion and there is a large velocity slip between the phases.

$x^* = 1$: In the transition region, significant changes in the flow properties take place. Indeed, the interaction between the both phases causes the particles to slow down while the gas accelerates. The flow is characterized by a non-equilibrium state in this region.

$x^* = 5$: In the far downstream region, the particles have enough time to approach the state of the gas motion. The slip is very small and the solution tends to equilibrium.

These results are in good agreement with analytical and numerical solutions proposed by all the authors who contributed earlier to this topic. Wang and Glass [14] developed the series

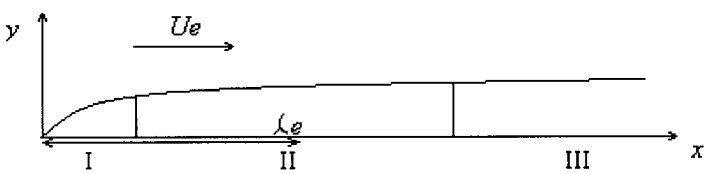

Figure 13. Boundary layer over a flat plate.

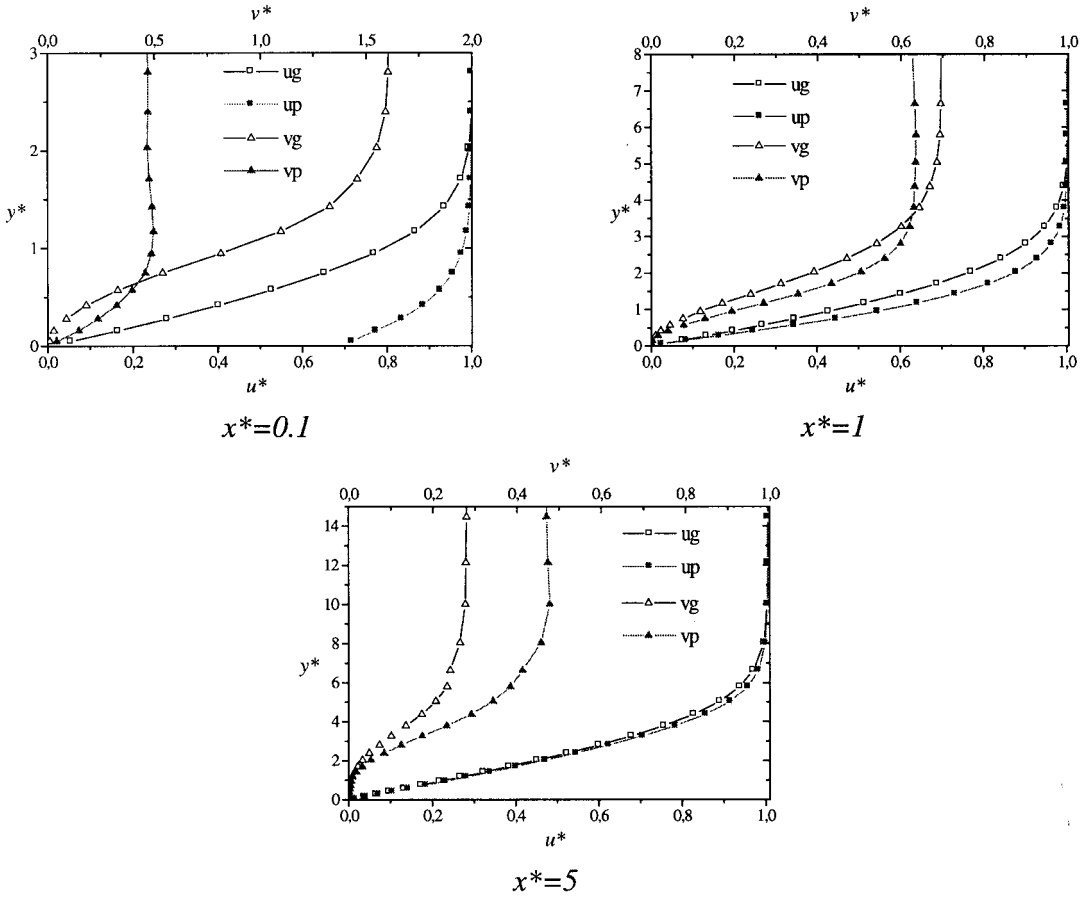

Figure 14. Velocity profiles in the boundary layer.

expansion method used by Singleton [13] and obtained the characteristics of a compressible flow in the large- and small-slip region. They also defined a finite difference method and obtained numerical results similar to those mentioned in the present paper for the three regions of the flow. These results were accorded the asymptotic ones and gave an accurate description of the transition region. But their numerical scheme could only solve simplified equations of the boundary layer and done it in an implicit way. The improvement brought by the MUSCL–Hancock scheme lies on the suppression of these limitations.

It is interesting to observe the influence of the mass loading ratio $\alpha = \rho_{p,e}/\rho_e$ on some flow characteristics. Figure 15 shows the dependence of the local skin friction factor on the load factor for a steady flow. Re_x is defined as the Reynolds number based on the distance x from the leading edge and the group $C_f Re_x^{1/2}$ is plotted against x^*. The higher α is, the more important the stress on the plate is. The particles give kinetic energy to the gas, which accelerates in the boundary layer. Hence, the velocity gradients increase leading to a thinner boundary layer than in a pure gas flow. Consequently, the stress on the wall is stronger. This one reaches a maximum in the moderate-slip region at the critical point corresponding to the transition from the non-equilibrium flow to the equilibrium flow.

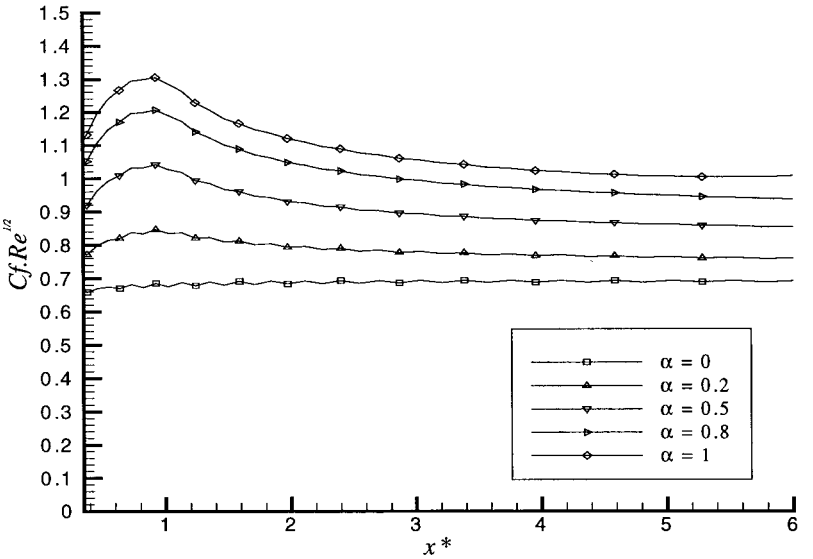

Figure 15. Skin friction factor.

This test shows that the scheme is perfectly able to simulate two-phase boundary layers. Nevertheless, as was pointed out by Chamkha and Peddieson [16], the dusty gas model reaches a limit in this particular case. Indeed, as shown in Figure 16 at $t = 1$ ms, the particle phase density increases at one relaxation length from the leading edge and becomes infinite for a steady flow, which is inconsistent with the model hypothesis and observed physical behaviours. It is, therefore, interesting to use more elaborate models incorporating ideas similar to those discussed by Soo [15]. These models endow the particle phase with diffusion and viscosity but numerous factors have to be experimentally determined. One has to take care by using the dusty gas model in this kind of flows.

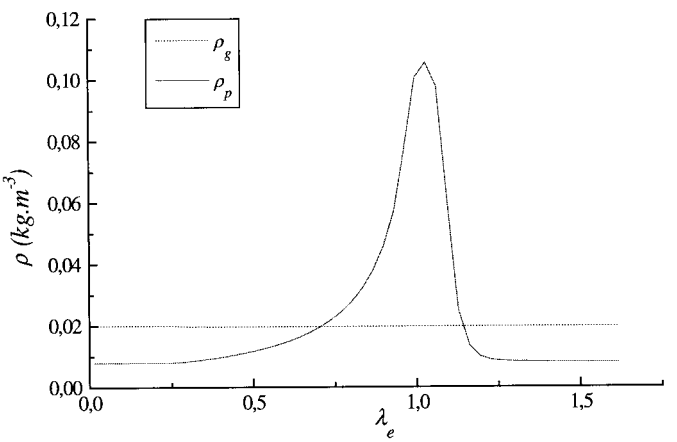

Figure 16. Particle density at the wall.

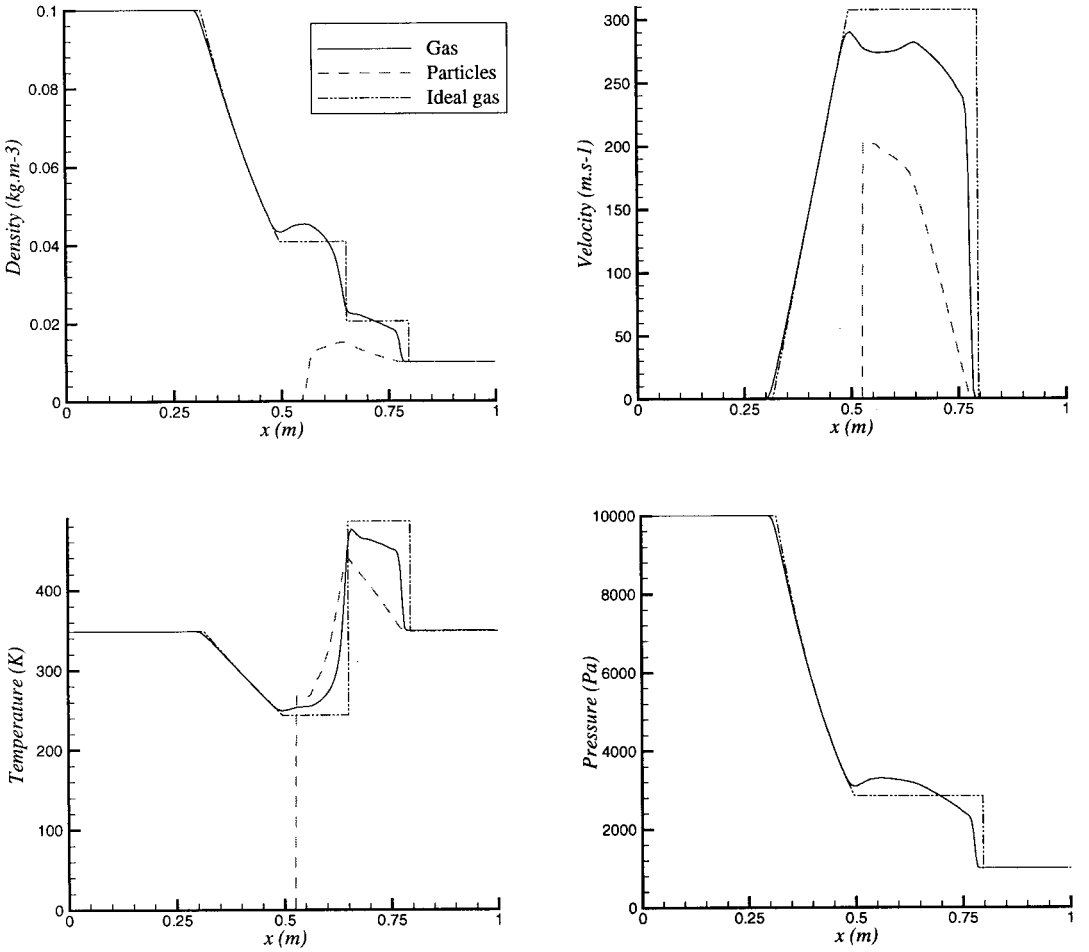

Figure 17. External flow characteristics in a two-phase shock tube.

4.5. *Non-stationary two-phase flow in a shock tube*

Miura and Glass [32] analytically and numerically investigated the flow in a shock tube with suspended small solid particles. In this study, the Euler equations described the gas phase behaviour. Hereafter, their results are drawn from to validate the scheme for the simulation of unsteady two-phase flows. In the following simulation, the pressure in the low-pressure section of the shock tube is higher than for the test case developed for the validation of the one-phase flow computation. Consequently, the boundary layer is thinner and the external flow can be directly compared with the solution obtained for an inviscid flow. The pressure ratio is equal to 10. The temperature is set to the same value in both sections. The particles are only present in the low-pressure section, where the shock front and the contact surface will propagate. The particle diameter is equal to 10 μm and the density ratio $\alpha = \rho_{p,e}/\rho_e$ is equal to 1. The gas and the particles are initially under thermal and dynamical equilibrium conditions. The computational mesh is the same as that used for the one-phase flow shock tube calculation. The slope limiter used for the gas phase, as well as the particle phase, is the Van-Leer limiter.

Some flow quantities in the external flow are shown in Figure 17 at time $t = 0.5$ ms. The dotted lines represent the exact solution for an inviscid one-phase flow. The solid lines show the characteristics of the gas phase in the present case. The evolutions of the particle density, velocity and temperature are also depicted (dashed lines).

One can notice that the velocity of the shock wave as well as the contact surface diminishes by comparison with a pure gas flow. The interaction with particles causes the gas to slow down and lose energy. The pressure increases between the shock front and the expansion fan and reaches a higher value then for a pure gas flow. As a result, the rarefaction wave weakens.

Considering the dispersed phase, one can observe that it cannot follow the sudden change in the carrier phase: the particle velocity and temperature rise gradually because of the gas interaction through the shock wave. The particle concentration increases gradually from the shock front to the contact surface, then drops to zero. The positive property of the particle solver is necessary in such a case so as to avoid negative values. Some particles cross the contact surface and heat the gas, which explains the increase of gas temperature in this region.

These results are in perfect agreement with the numerical results provided by Miura and Glass [32], who have drawn on experimental observations. Figure 18 shows the particle phase characteristics in the whole computation domain at time $t = 0.5$ ms. One can also follow the evolution of the particle density, velocity and temperature in the boundary layer. In this area, the kinetic energy given to the particles decreases between the external flow and the wall then the particle velocity remains low near the wall. The particles heating between the shock front and the contact discontinuity increases in the boundary layer due to the thermal energy gained from the work of shear stress forces in the gas phase.

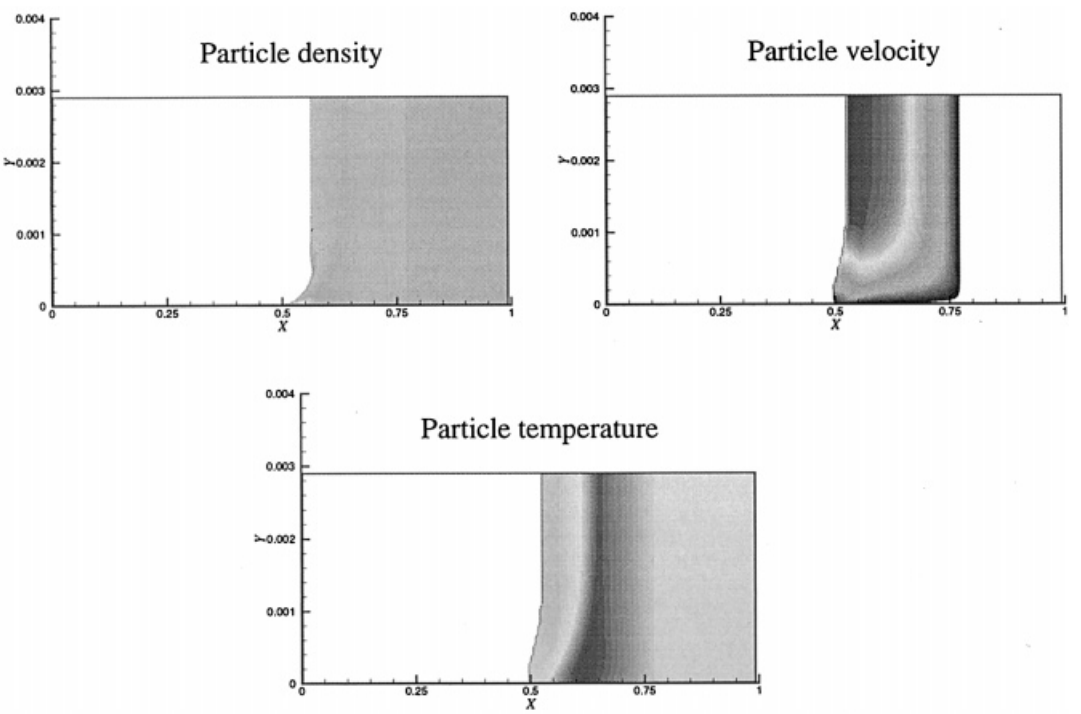

Figure 18. Particle phase characteristics.

The fact that the MUSCL–Hancock scheme is able to simulate unsteady viscous two-phase flow is now verified.

5. CONCLUSIONS

An efficient numerical method for the solution of unsteady two-phase viscous flows is presented. The equations solved are based on the assumption of a dilute particle flow considered as a continuum media. The methodology is based on a finite volume TVD scheme in which the fluxes are computed by exact Riemann solvers. The method is extended to solve the gaseous and the dispersed phase in the same way. It is noticeable that this kind of method is largely used in the CFD community for the gaseous flow but is quite unusual for two-phase viscous flows. Then a careful validation of the method was made step-by-step, starting from steady one-phase viscous flows and finishing with unsteady two-phase viscous flows. At each step, we take care to confront the results with analytical or numerical results. The agreement is quite good and allows quite a powerful numerical tool for the solution of such flows to be obtained. Then some more physical studies can be considered in future works, such as the interaction between particles and boundary layers or unsteady applications in shock tubes. Moreover, there is no evident limit to incorporate more sophisticated models in the numerical method, such as the diffusivity effects in the particle phase pointed out in previous works.

REFERENCES

1. J. Sabnis, F. de Jonc and H. Gibeling, 'A two-phase restricted equilibrium model for combustion of metalized solid propellants', *AIAA Paper 92-3509*, 1992.
2. P. Liaw and Y.S. Chen, 'Particulate multiphase flow field calculation with combustion, break-up models for solid rocket motor', *AIAA Paper 94-2780*, 1994.
3. I.S. Chang, 'One- and two-phase nozzle flows', *AIAA J.*, **18**, 1455–1461 (1980).
4. E. Daniel, R. Saurel, M. Larini and J.C. Loraud, 'A multiphase formulation for two-phase flows', *Int. J. Heat Fluid Flow*, **4**, 269–280 (1994).
5. R. Saurel, E. Daniel and J.C. Loraud, 'Two-phase flows: second-order schemes and boundary conditions', *AIAA J.*, **32**, 1214–1221 (1994).
6. E. Daniel, T. Basset and J.C. Loraud, 'Eulerian approach for unsteady two-phase reactive, solid rocket motor flows loaded with aluminum particles', *34th AIAA/ASME/SAE/ASEE Joint Propulsion Conf.*, Cleveland, OH, July 13–15, 1998.
7. E. Daniel, T. Basset and J.C. Loraud, 'Combustion of aluminum particles in two-phase reactive solid rocket motor', *3rd Int. Conf. on Multiphase Flow*, Lyon, France, June 8–12, 1998.
8. F.E. Marble, 'Dynamics of a gas containing small solid particles', *Combustion and Propulsion, 5th AGARD Colloquium*, Pergamon Press, Oxford, 1963.
9. S.L. Soo, *Fluid Dynamics of Multiphase Systems*, Blaisdell, Waltham, 1967.
10. J.T.C. Liu, 'Flow induced by the impulsive motion of an infinite plate in a dusty gas', *Astronaut. Acta.*, **13**, 369 (1967).
11. A.N. Osiptsov, 'Structure of the laminar boundary layer of a disperse medium on a flat plate', *Fluid Dyn.*, **15**, 512–517 (1980).
12. S. Prabha and A.C. Jain, 'On the use of compatibility conditions in the solution of gas particulate boundary layer equations', *Appl. Sci. Res.*, **36**, 81–91 (1980).
13. R.E. Singleton, 'The incompressible gas solid particle flows over a semi-infinite flat plate', *Z. Angew Math. Phys.*, **19**, 545 (1965).
14. B.Y. Wang and I.I. Glass, 'Compressible laminar boundary layer flows of a dusty gas over a semi-infinite flat plate', *J. Fluid Mech.*, **186**, 223–241 (1988).
15. S.L. Soo, 'Boundary layer motion of a gas–solids suspension', *Proc. Symp. Interaction between Fluids and Particles*, *Inst. Chem. Eng.*, pp. 50–63 (1962).
16. A.J. Chamkha and J.J.R. Peddieson, 'Boundary layer flow of a particulate suspension past a flat plate', *Int. J. Multiphase Flow*, **17**, 805–808 (1991).
17. N. Lupoglazoff and F. Vuillot, 'Numerical simulation of non-steady two-dimensional flows in solid propellant propulsion system', *La Recherche Aerospatiale*, **2**, 21–41 (1992).

18. F. Vuillot, T. Basset, J. Dupays, E. Daniel and N. Lupoglazoff, '2D Navier–Stokes stability computation for solid rocket motors: rotational, combustion and two-phase flow effects', *AIAA Paper 97-3326*, 1997.
19. L. Sainseaulieu, 'Finite volume approximation of two-phase fluid flows based on an approximate Roe-type Riemann solver', *J. Comput. Phys.*, **121**, 1–28 (1995).
20. B. Van-Leer, 'MUSCL, a new approach to numerical gas dynamic', *Computing in Plasma Physics and Astrophysics*, Max–Plank Institut für Plasma Physik, Germany, 1976.
21. B. Van-Leer, 'Toward the ultimate conservative difference scheme IV. A second-order sequel to Godunov's method', *J. Comput. Phys.*, **32**, 101–136 (1979).
22. E.F. Toro, *Riemann Solvers and Upwind Methods for Fluid Dynamics*, Springer, Berlin, 1997.
23. R. Ishii, Y. Umeda and M. Yuhi, 'Numerical analysis of gas–particle two-phase flows', *J. Fluid Mech.*, **203**, 475–515 (1989).
24. S.M. Dash and R.D. Thorpe, 'Shock capturing model for one- and two-phase supersonic exhaust flow', *AIAA J.*, **19**, 842–851 (1980).
25. M. Gilbert, L. Davis and D. Altman, 'Velocity lag of particles in linearly accelerated combustion gases', *Jet Propul.*, **25**, 26–30 (1955).
26. J.G. Knudsen and D.L. Katz, *Fluid Mechanics and Heat Transfer*, Hemisphere, New York, 1958.
27. C. Hirsch, *Numerical Computation of Internal and External Flows*, Wiley, New York, 1988.
28. P.A. Jacobs 'Single-block Navier–Stokes integrator', *ICASE Report*, 1991.
29. H. Blasius, 'Grenzschichten in flüssigkeiten mit kleiner reibung', *Z. Math. Phys.*, **56**, 1–37 (1905).
30. J. Cousteix, *Couche Limite Laminaire*, Cepadues-Editions, 1988.
31. H. Mirels, 'Test time in low pressure shock tubes', *Phys. Fluid.*, **6**, 9 (1963).
32. H. Miura and I.I. Glass, 'On a dusty gas shock tube', *Proc. R. Soc. Lond.*, **A382**, 373–388 (1982).

